Article

Ti-40Al-10Nb-10Cr Porous Microfiltration Membrane with Hierarchical Pore Structure for Particulate Matter Capturing from High-Temperature Flue Gas

Wanyuan Gui [1], Zhenjing Shi [2], Yin Zhang [3], Yongfeng Liang [2], Jingyan Qin [4], Yanli Wang [2], Junpin Lin [2,*] and Benli Luan [1,5,*]

1   National Center for Materials Service Safety, University of Science and Technology Beijing, Beijing 100083, China; guiwy@ustb.edu.cn
2   State Key Laboratory for Advanced Metals and Materials, University of Science and Technology Beijing, Beijing 100083, China; s20201214@xs.ustb.edu.cn (Z.S.); liangyf@skl.ustb.edu.cn (Y.L.); wan-gyl@ustb.edu.cn (Y.W.)
3   Xi'an Thermal Power Research Institute Co., Ltd., Xi'an 100083, China; yinzhang330@163.com
4   School of Mechanical Engineering, University of Science and Technology Beijing, Beijing 100083, China; qin-jingyanking@foxmail.com
5   Department of Chemistry, Western University, London, ON N6A 5B7, Canada
*   Correspondence: linjunpin@ustb.edu.cn (J.L.); bluan@ustb.edu.cn (B.L.)

Abstract: TiAl-based porous microfiltration membranes are expected to be the next-generation filtration materials for potential applications in high-temperature flue gas separation in corrosive environments. Unfortunately, the insufficient high-temperature oxidation resistance severely limits their industrial applications. To tackle this issue, a Ti-40Al-10Nb-10Cr porous alloy was fabricated for highly effective high-temperature flue gas purification. Benefited from microstructural changes and the formation of two new phases, the Ti-40Al-10Nb-10Cr porous alloy demonstrated favorable high-temperature anti-oxidation performance with the incorporation of Nb and Cr high-temperature alloying elements. By the separation of a simulated high-temperature flue gas, we achieved an ultra-high PM-removal efficiency (62.242% for $PM_{<2.5}$ and 98.563% for $PM_{>2.5}$). These features, combined with our experimental design strategy, provide a new insight into designing high-temperature TiAl-based porous materials with enhanced performance and durability.

Keywords: intermetallic; TiAl porous alloys; microfiltration membrane; separation and purification; high-temperature application

1. Introduction

The immense potential in energy conversion and storage, adsorption and separation applications has generated significant interest in the design and synthesis of hierarchically porous materials [1–5]. Hierarchically porous materials have many unique features, such as tunable porous structures, controllable macroscopic morphologies, a large surface area and an easily functionalizable surface, making them some of the most promising engineering structural materials [6–13]. High-temperature flue gases discharged from electric power, petroleum, chemical and metallurgical operations have the characteristics of high temperature (above 800 °C), high oxygen content, high sulfur content, high nitrogen content and large amounts of dust content [7–9]. Dust removal from these high-temperature flue gases remains a major challenge due to the formation of blockage caused by particle-containing high-temperature flue gases and the corrosion of dust removal equipment. Porous metals [14,15] and porous ceramics [16–19] are widely utilized where high-temperature flue gas is initially released to take full advantage of the filtration efficiency. Unfortunately, the poor oxidation resistivity, poor corrosion resistance and intolerance at elevated temperatures of porous metals and the severe brittleness, poor thermal vibration resistance and

unworkability of porous ceramics have severally restricted their potential applications in high-temperature flue gas purification. As such, it is of considerable significance to develop functional porous materials for high-temperature flue gas purification with a simple, highly efficient and scalable approach.

TiAl-based porous materials have been very promising candidates as high-temperature structural materials for high-temperature flue gas purification, because they contain a mixture of metallic and covalent bonds that provide sound mechanical properties with outstanding corrosion resistance and excellent oxidation resistance above 600 °C [20–23]. However, TiAl-based porous materials still need to be improved, owing to the insufficient oxidation resistance in the envisioned application temperature range of 800 °C–1000 °C. The main reason for the inadequate performance is related to the formation of both TiO_2 and Al_2O_3 rather than continuous Al_2O_3 during long-term high-temperature oxidation [19,24–26]. For example, the oxidation products of a binary γ-TiAl isothermally oxidized at 1000 °C for 48 h include not only Al_2O_3 (α-alumina), but also TiO_2 (rutile titanium dioxide), TiN, Ti_2AlN and $α_2$-Ti_3Al [27]. More specifically, the oxide scale of TiAl alloys generally consists of three layers, an outer layer of TiO_2, an intermediate layer of Al_2O_3 and a porous inner layer consisting of TiO_2 and Al_2O_3 grains. A great deal of research has already been conducted to enhance the anti-oxidation resistance of TiAl-based alloys above 800 °C through the addition of ternary and quaternary alloy elements into TiAl-based alloys, such as Nb [28], Ta [29], Ni [30], Y [31], B [16], Si [32], W [33] and Mo [34], either to form a protective scale or to slow down the oxygen diffusion rate. However, these studies are still at the experimental stages based on bulk TiAl-based alloys. It is still unclear whether or not the benefits would apply to TiAl-based porous alloys, particularly in controlling the surface morphology and pore parameters. The alloy design should be highly effective in improving high-temperature corrosion resistance without compromising the pore parameters. As such, the development of a simple and effective method to substantially improve the high-temperature oxidation resistance of TiAl-based materials while maintaining the desired porous structures is much needed.

The main objective of this study is to fabricate a novel TiAl-based porous material with the addition of Nb and Cr elements for high-temperature applications. The formation mechanism of the new porous material was investigated and the effects of Nb and Cr doping into the TiAl porous alloy were also demonstrated. Furthermore, the enhancement of anti-oxidation resistance was studied through the characterization analyses before and after high-temperature oxidation at 900 °C for 100 h. This new research project resulted in a new TiAl-based material with good high-temperature oxidation resistance and excellently structural stability for high-temperature PM capturing.

2. Experimental Section

2.1. Materials

The chemical composition of all samples are as follows: commercial Ti, Al, Nb and Cr powders with a purity of 99.9% and an average particle size of less than 50 μm. All these powders were supplied by DK nano technology Co. Ltd., Beijing, China.

2.2. Instruments

The morphological features of the Ti-48Al, Ti-48Al-6Nb, Ti-48Al-2Nb-2Cr and Ti-40Al-10Nb-10Cr porous materials were observed with a field emission scanning electron microscopy (FESEM, ZEISS SUPRA 55, Carl Zeiss, Germany), while the compositional analyses of the samples were performed using energy dispersion spectrometry (EDS). X-ray diffraction (XRD; Multipurpose X-ray Diffractometer TTR III, Rigaku Co., Tokyo, Japan) was used for phase analysis. The pore structure was examined by FESEM and the pore parameters were measured by mercury intrusion porosimetry (MIP; Quantachrome AUTOSCAN-33, Boynton Beach, Florida, USA).

2.3. Preparation Process of TiAl-Based Porous Materials

In the preparation process of TiAl-based porous materials, as shown in Figure 1, commercial Ti, Al, Nb and Cr powders with the molar ratios of 52:48, 46:48:6, 48:48:2:2 and 40:40:10:10 were mixed, followed by ball milling at 120 rpm in a ball crusher for 24 h (ball-to-powder weight ratio of 4:1) and the mixtures were subsequently pressed into green pellets with a diameter of 30 mm under the pressure of 230 MPa. A four-step heat-treatment process in a vacuum was then conducted to fabricate TiAl-based porous materials. More specifically, the pellets were heated at 120 °C/1 h for vapor evaporation, at 600 °C/3 h and 900 °C/3 h for the Al and Ti reaction, Al and Nb reaction and phase transformation and, finally, at 1350 °C/3 h to form the TiAl-based porous materials.

2.4. High-Temperature Oxidation of TiAl-Based Porous Materials

To study the thermal cycling oxidation behavior, the Ti-48Al, Ti-48Al-6Nb, Ti-48Al-2Nb-2Cr and Ti-40Al-10Nb-10Cr porous alloys were treated at 900 °C for a total oxidation duration of 100 h. In detail, all the TiAl-based porous materials samples were kept at 900 °C for high-temperature oxidation, removed from the furnace with various oxidation intervals (2 h, 6 h, 10 h, 20 h, 30 h, 40 h, 50 h, 60 h, 70 h, 80 h, 90 h and 100 h), cooled in air (at room temperature) for 1 h for weighing and then placed back in the furnace for continued oxidation for 100 h. Besides weight measurements, FESEM was performed after thermal cycling oxidation treatment.

2.5. High-Temperature Filtration Performance of Ti-40Al-10Nb-10Cr Porous Alloy Tests

A home-made high-temperature PM filtration apparatus was applied to evaluate the filtration performance of the Ti-40Al-10Nb-10Cr porous alloys. The PM in the high-temperature PM filtration apparatus was generated by burning incense [35], while the size and concentration of PM before and after filtration were measured by two laser PM sensors (DT9881, CEM). The simulated high-temperature pollutant gas flowing through the Ti-40Al-10Nb-10Cr porous alloys samples (sample specifications: $\Phi30 \times 0.6$ mm, with an effective area of about 706.5 mm^2) was placed inside a quartz tube in a furnace (900 °C, 3000 Pa). Two PM counters were placed at the downstream and upstream of the testing samples, respectively, to measure the PM number before and after filtration. During the experiment, high-temperature PM-containing air flowed at a 2 L/min constant rate through the samples. Three Ti-40Al-10Nb-10Cr porous alloys samples were tested to ensure filtration measurement accuracy. Their removal efficiency was calculated by Equation (1) as follows:

$$\eta = (1 - \xi_1/\xi_2) \times 100\% \tag{1}$$

where ξ_1 and ξ_2 represent the concentrations of incense PM in the downstream and upstream of the filter, respectively.
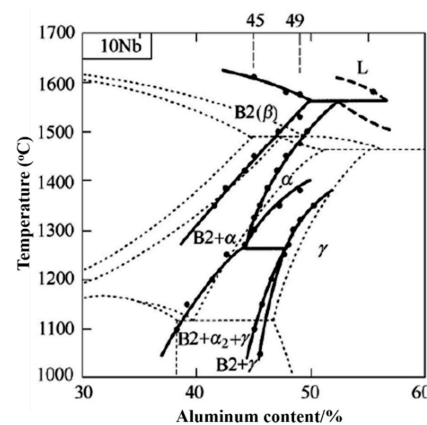

Figure 1. Phase diagram of TiAl binary phase diagram (dashed line) and Ti-40Al alloy with 10Nb (solid line) [36].

3. Results and Discussion

3.1. Phase Composition and Microstructure of TiAl-Based Porous Materials

Figure 1 depicts the typical TiAl binary phase diagram (dashed line) and preliminary phase diagram of TiAl with 10Nb (solid line), respectively. It can be observed that, with a 10 at% Nb addition, the phase diagram of TiAl changed. The melting point of the TiAl alloy increased by about 80~100 °C; the phase transition point (β/β+α) was reduced by about 50~80 °C and the phase region was enlarged and extended to the high Al region; the α(α/α+γ) transition point decreased by about 30 °C; the β+α/α transition temperature decreased by about 50~100 °C; the α single-phase region was compressed and moved to high Al content; the γ phase region extended to low Al content; the maximum solubility of Nb in the α_2 and γ phases was about 9.5 at% [36]. In addition, Tang and Shemet suggested that whether addition of Cr does good or harm to a TiAl alloy depends on the amounts used; with less-than-4 at% Cr additions, Cr occupied the position of Ti in TiO_2 in the form of +3 valence, which was harmful to the oxidation resistance. However, with 8 at%~10 at% Cr additions, Cr could promote the formation of an Al_2O_3 film and was beneficial to the improvement of antioxidation properties [37]. Therefore, Ti-40Al-10Nb-10Cr was selected as the composition with consideration of the effects of both Nb and Cr on the oxidation resistance for high-temperature applications.

The XRD patterns obtained from the surfaces of the Ti-48Al, Ti-48Al-6Nb, Ti-48Al-2Nb-2Cr and Ti-40Al-10Nb-10Cr specimens are shown in Figure 2. The Ti-48Al porous alloys were mainly composed of Ti_3Al and TiAl. Besides Ti_3Al and TiAl, two new phases, $NbAl_3$ and Nb_2Al, were detected in the Ti-48Al-6Nb and Ti-48Al-2Nb-2Cr samples. In addition, the new phase B2 was also found in Ti-40Al-10Nb-10Cr porous alloys. These findings are similar to the results of our previous study [23,38].
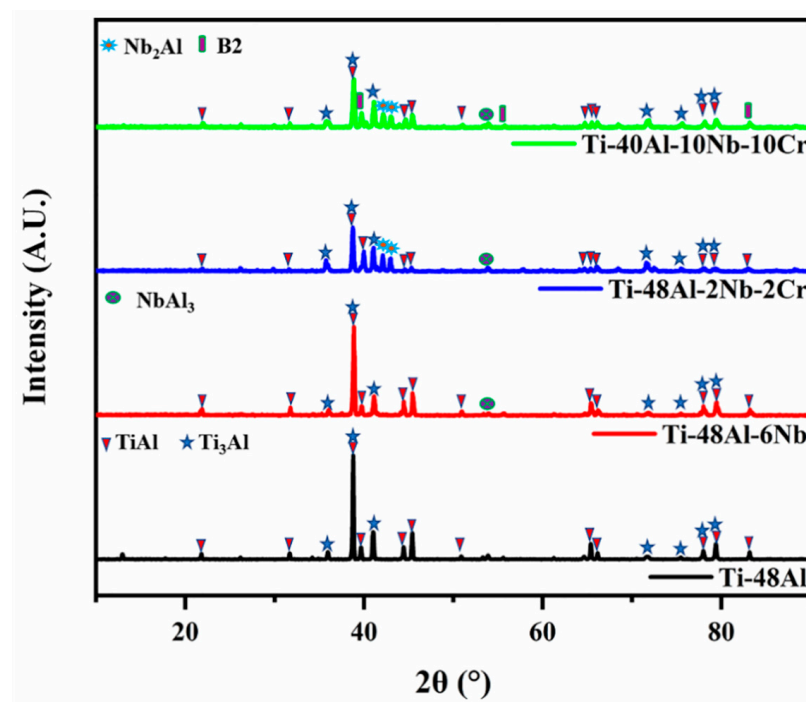

Figure 2. XRD patterns of TiAl-based porous materials: Ti-48Al (black), Ti-48Al-6Nb (red), Ti-48Al-2Nb-2Cr (blue) and Ti-40Al-10Nb-10Cr (green).

Figure 3a depicts typical FESEM images of Ti-48Al porous materials. The results show that Ti-48Al porous materials mainly consisted of irregular spherical particles, leading to a hierarchically porous skeleton (funnel-shaped with big pore mouth and small pore throat). There existed a lot of pores with different pore diameters among the Ti-48Al skeletons. Compared with Ti-48Al porous materials, a larger number of white irregular

particles appeared on the surface of the Ti-48Al-6Nb, Ti-48Al-2Nb-2Cr and Ti-40Al-10Nb-10Cr porous alloys, due to the presence of high Nb phases ($NbAl_3$ and Nb_2Al) and the B2 phase, as shown in Figure 3b–d. In particular, a larger number of irregular particles appeared around the pores of the Ti-40Al-10Nb-10Cr samples, resulting in the formation of an increasing number of small pores on the hierarchically porous skeleton.
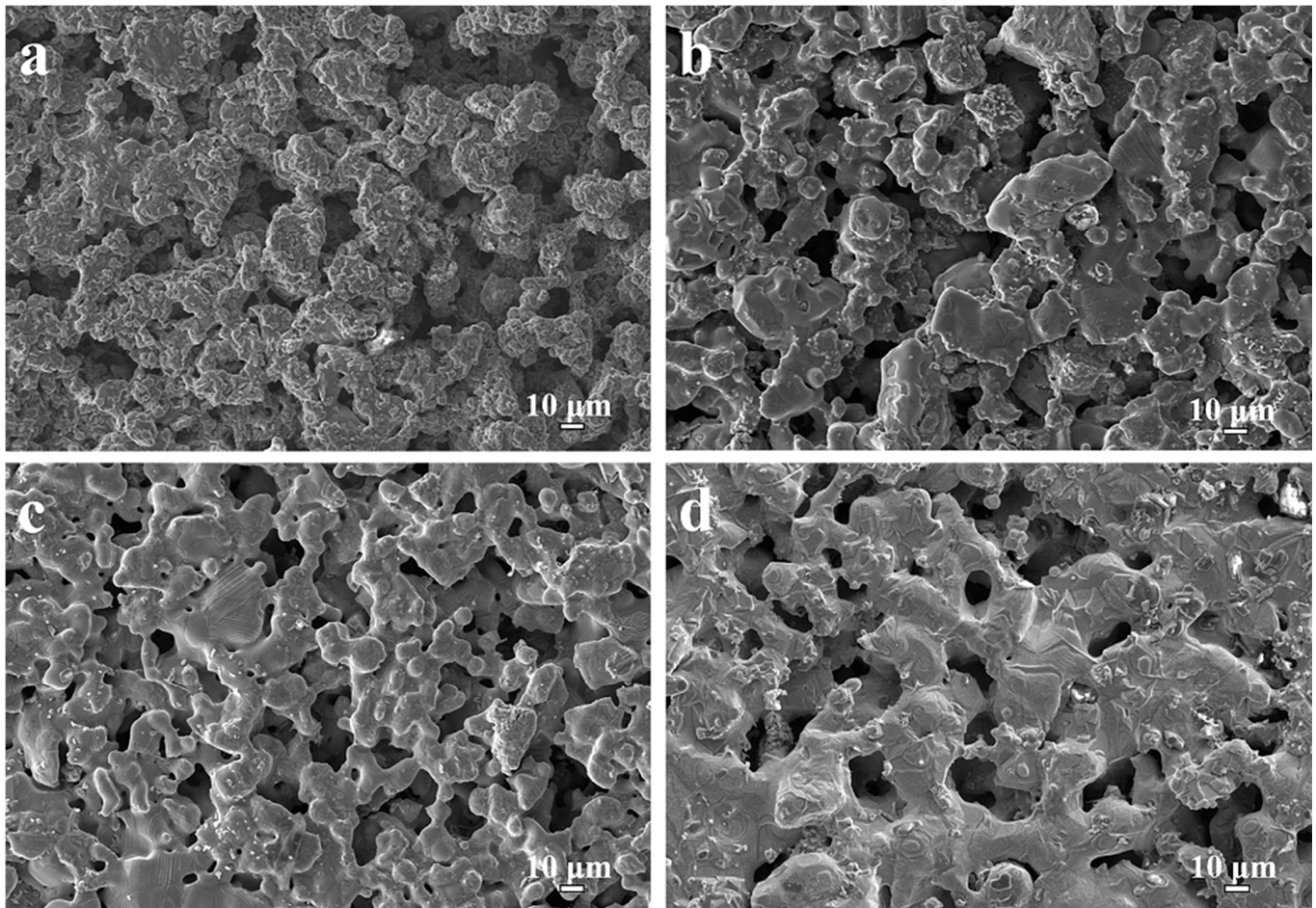

Figure 3. Skeleton surface morphologies of TiAl-based porous alloys: (**a**) Ti-48Al, (**b**) Ti-48Al-6Nb, (**c**) Ti-48Al-2Nb-2Cr and (**d**) Ti-40Al-10Nb-10Cr.

3.2. Pore Parameters of TiAl-Based Porous Materials

Although the SEM images clearly showed the presence of pore mouths with, predominantly, the size of 20–50 μm, the size of pore throats was less than 10 μm, which made the MIP method still applicable [39] and the pore diameter distribution of the TiAl-based porous alloys were analyzed accordingly, as depicted in Figure 4. As for the Ti-48Al porous alloy, an average pore diameter of 8.319 μm was observed from a Gaussian distribution, with the peak position of the pore diameter occurring around 9.185 μm, 9.376 μm and 10.248 μm for the Ti-48Al-6Nb, Ti-48Al-2Nb-2Cr and Ti-40Al-10Nb-10Cr samples, respectively. Smaller peaks of pore diameters at 2–5 μm for the Ti-48Al, Ti-48Al-6Nb and Ti-48Al-2Nb-2Cr porous alloys and 0–2 μm for the Ti-40Al-10Nb-10Cr porous alloy were also observed, demonstrating a wide range of pore diameter distribution for TiAl-based porous alloys. In addition, detailed pore parameters of the TiAl-based porous alloys are given in Table 1. Compared to the Ti-48Al porous alloy, the pore area and pore volume of the Ti-48Al-6Nb, Ti-48Al-2Nb-2Cr and Ti-40Al-10Nb-10Cr porous alloy all decreased to a different extent, due to their wider pore diameter distribution. After Nb and Cr additions, the porosity increased, except for the Ti-48Al-2Nb-2Cr porous alloy. In addition, the porous skeletons increased due to an increase in the apparent skeletal density. The appearance of

the high Nb phase (NbAl$_3$ and Nb$_2$Al phase) and B2 phase indicated an increase in the Ti-48Al-6Nb, Ti-48Al-2Nb-2Cr and Ti-40Al-10Nb-10Cr porous alloys' skeletons.
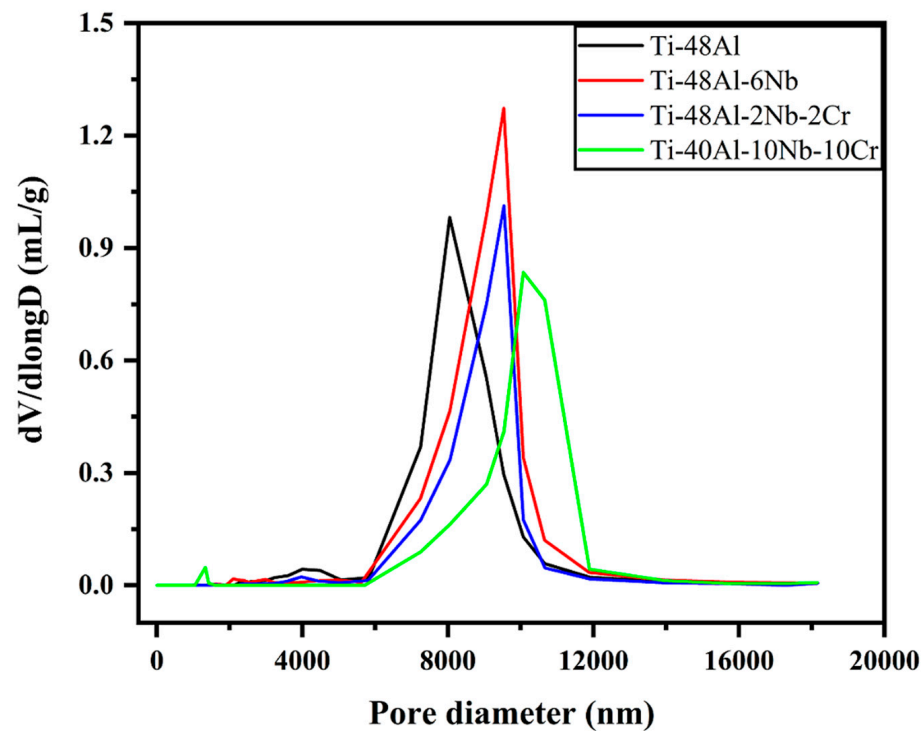

Figure 4. Pore diameter distribution curves of TiAl-based porous materials: Ti-48Al (black), Ti-48Al-6Nb (red), Ti-48Al-2Nb-2Cr (blue) and Ti-40Al-10Nb-10Cr (green).

Table 1. Pore parameters of the TiAl-based porous materials.

Samples	Total Pore Volume (cm^3/g)	Total Pore Area (m^2/g)	Bulk Density (g/cm^3)	Porosity (%)
Ti-48Al	0.113 ± 0.008	0.055 ± 0.007	3.683 ± 0.122	29.445 ± 0.054
Ti-48Al-6Nb	0.118 ± 0.013	0.052 ± 0.011	3.749 ± 0.134	30.577 ± 0.069
Ti-48Al-2Nb-2Cr	0.082 ± 0.005	0.038 ± 0.007	4.644 ± 0.095	27.551 ± 0.038
Ti-40Al-10Nb-10Cr	0.097 ± 0.003	0.040 ± 0.001	4.358 ± 0.037	29.805 ± 0.003

3.3. High-Temperature Oxidation Performance

Figure 5 shows the effect of Nb and Cr elemental additions on the high-temperature oxidation behavior of TiAl-based porous alloys. As was measured, the Ti-48Al porous alloys showed a weight gain of 27.39 g/m^2 after a thermal cycling treatment at 900 °C for 100 h. Compared to Ti-48Al porous alloys, all the TiAl-based porous alloys after Nb and Cr addition showed a lower oxidation rate, especially the Ti-40Al-10Nb-10Cr sample, with a minimum weight gain of 6.55 g/m^2. The great improvement of the high-temperature oxidation resistance achieved through the addition of Nb and Cr powders could be explained by the barriers towards the formation of TiO$_2$ due to the presence of high Nb phases (NbAl$_3$ and NbAl$_2$) and B2 phases. More specifically, the presence of the high Nb phases (NbAl$_3$ and Nb$_2$Al) and B2 phases could act as diffusion barriers, inhibiting the O inward diffusion and the Ti outward diffusion.
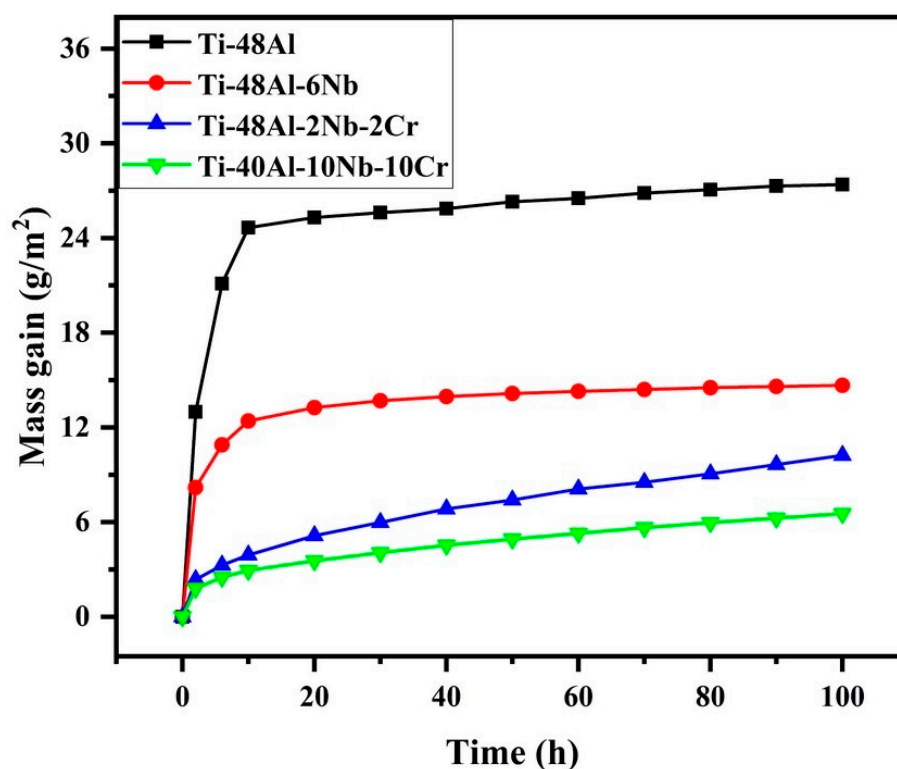
Figure 5. High-temperature oxidation behavior of TiAl-based porous materials: Ti-48Al (black), Ti-48Al-6Nb (red), Ti-48Al-2Nb-2Cr (blue) and Ti-40Al-10Nb-10Cr (green).

Figure 6 shows the micro-pore changes in the TiAl-based porous alloys after 900 °C/100 h isothermal treatment. The Kirkendall voids were quickly removed due to the formation of irregular white TiO_2 on the surface of the treated Ti-48Al porous alloy, as shown in Figure 6a. Moreover, microcracks could be seen on the surface of the treated Ti-48Al-6Nb porous alloy, attributed possibly to the stress of the high degree of oxidation, as shown in Figure 6b. As for the treated Ti-48Al-2Nb-2Cr and Ti-40Al-10Nb-10Cr samples, little change was observable to its surface after 900 °C/100 h thermal cycling treatment, as shown in Figure 6c,d. The surface compositions of TiAl-based porous alloys after thermal cycling treatment are listed in Table 2. In comparison with the treated Ti-48Al porous alloys, the content of O reduced greatly, while Ti, Al and Nb increased. The results further suggest that, for the Ti-48Al-6Nb, Ti-48Al-2Nb-2Cr and Ti-40Al-10Nb-10Cr porous alloys, the formation of high Nb phases ($NbAl_3$ and $NbAl_2$) and B2 phases prevented the further formation of TiO_2 and Al_2O_3 during thermal cycling treatment. These results are consistent with their high-temperature oxidation results shown in Figure 5.

Table 2. EDS composition analysis of the surface scans of TiAl-based porous alloys after the thermal cycling treatment shown in Figure 5.

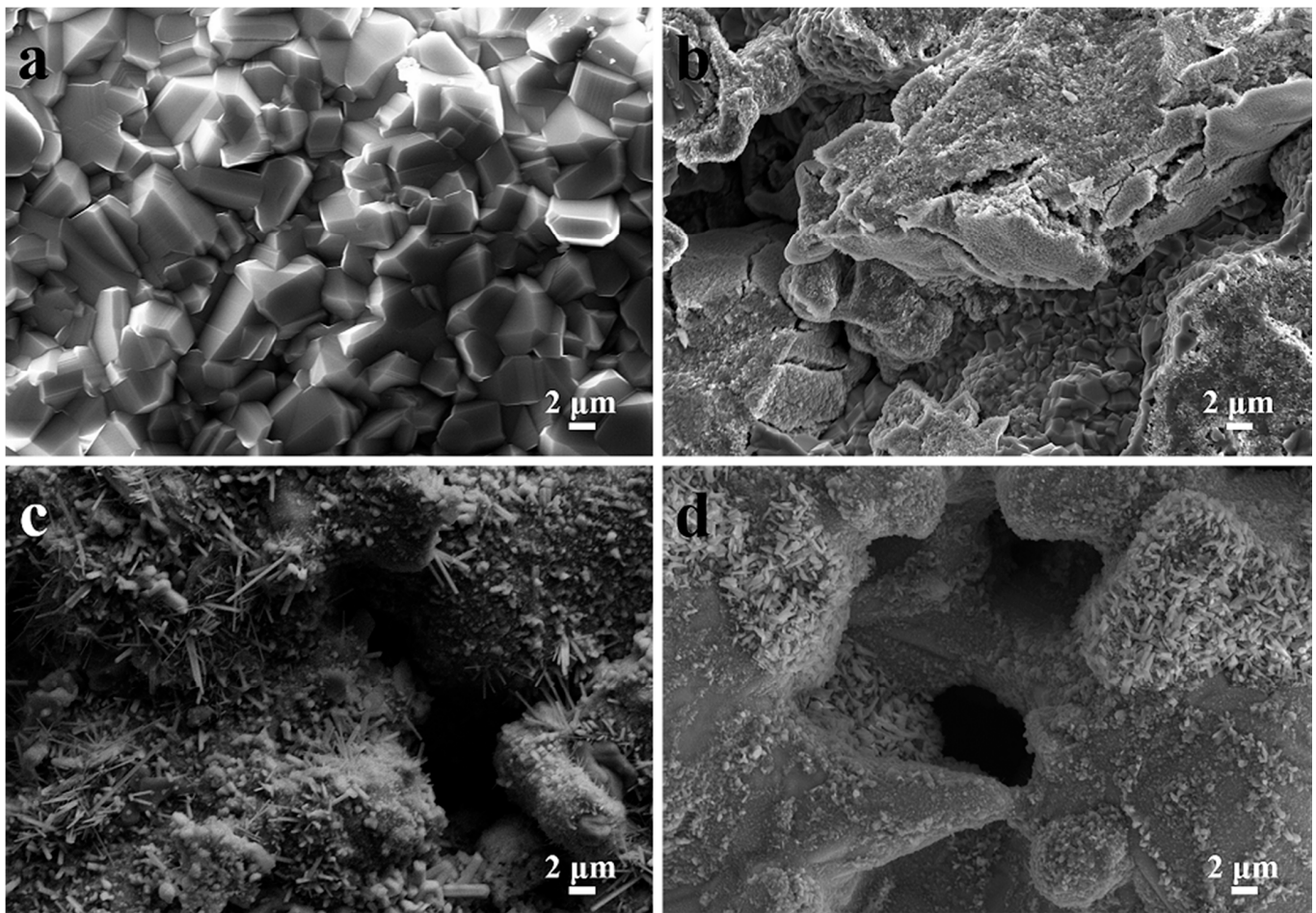| Samples	Ti	Al	Nb	Cr	O
Ti-48Al	32.96	0	0	0	67.04
Ti-48Al-6Nb	34.18	6.51	1.59	0	57.72
Ti-48Al-2Nb-2Cr	39.78	8.45	1.23	0.31	50.23
Ti-40Al-10Nb-10Cr	41.19	11.91	2.05	0.63	44.22

Figure 6. The SEM images of TiAl-based porous alloys after 900 °C/100 h thermal cycling treatment: (**a**) Ti-48Al, (**b**) Ti-48Al-6Nb, (**c**) Ti-48Al-2Nb-2Cr and (**d**) Ti-40Al-10Nb-10Cr.

The high-temperature PM filtration of Ti-40Al-10Nb-10Cr porous alloys was tested in the device shown in Figure 7a, with high-temperature PM (including $PM_{<2.5}$, $PM_{>2.5}$) filtered through Ti-40Al-10Nb-10Cr porous alloy. The $PM_{<2.5}$ and $PM_{>2.5}$ concentration after filtration using Ti-40Al-10Nb-10Cr porous alloys' filtration was much lower than the concentration before filtration (Figure 7b,c). The results shown in Figure 7d confirm that both high-temperature $PM_{<2.5\mu m}$ and $PM_{>2.5\mu m}$ could be filtered through the Ti-40Al-10Nb-10Cr membrane with a separation efficiency of 62.242% (SD: $\pm 1.099\%$) and 98.563% (SD: $\pm 0.449\%$), respectively. Furthermore, a comparison between Ti-40Al-10Nb-10Cr porous alloys and various porous materials in previous studies [2,19,40] shows that the Ti-40Al-10Nb-10Cr sample exhibited a relatively higher $PM_{>2.5\mu m}$ removal efficiency at a much higher pressure. It is of note that the upper limit of service temperature of as-prepared Ti-40Al-10Nb-10Cr porous alloys could survive a temperature of up to 900 °C. These results indicate that our Ti-40Al-10Nb-10Cr porous alloys could achieve flow-through filtration with high removal efficiency, showing great commercialization prospects for high-temperature PM filtration.
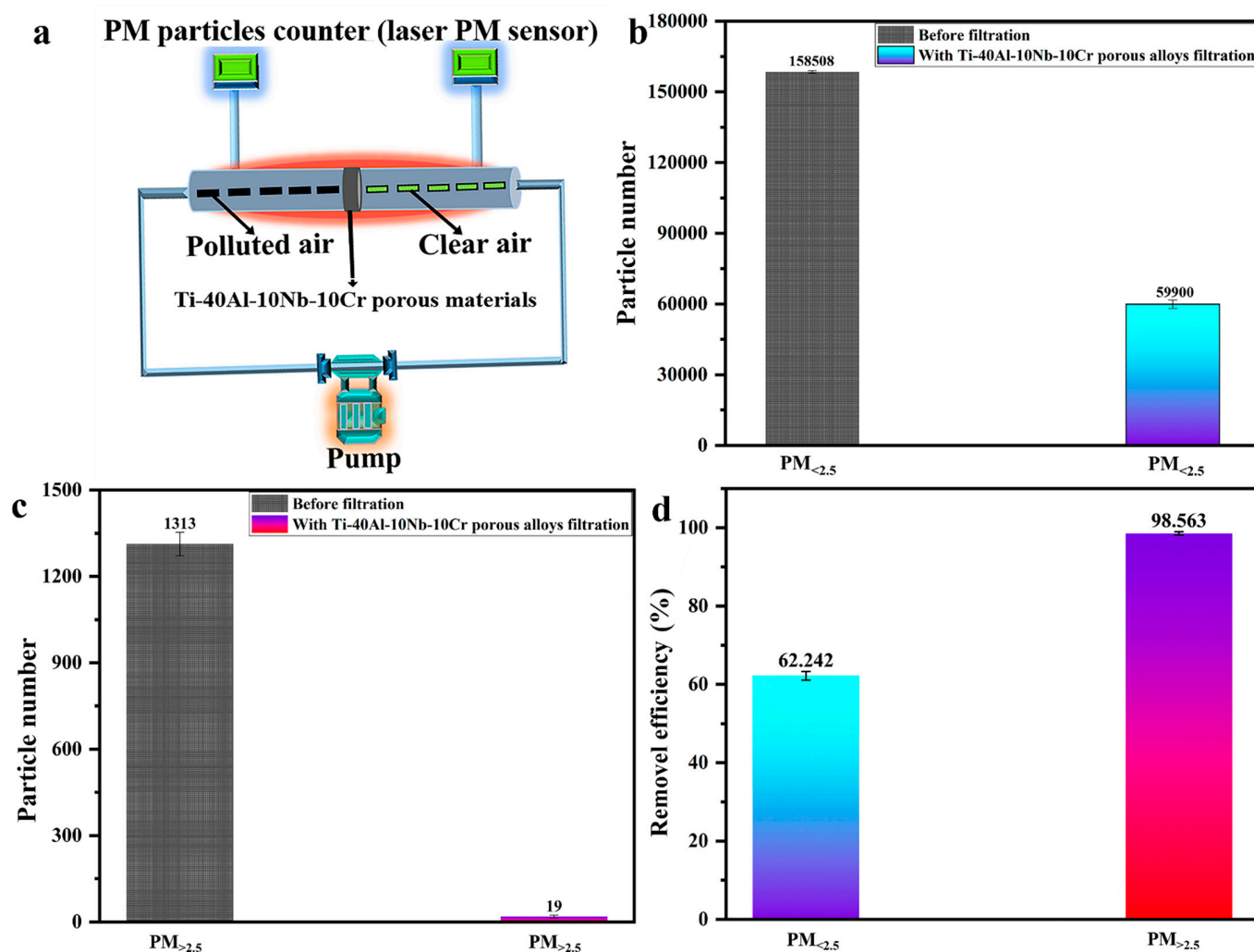
Figure 7. (**a**) Schematic of high-temperature PM filtration setup. (**b**,**c**) PM$_{<2.5}$ and PM$_{>2.5}$ concentration of dust-laden smoke (original) and after filtration under test condition. (**d**) Removal efficiency of Ti-40Al-10Nb-10Cr porous alloys after 60 min filtration test.

4. Conclusions

In conclusion, a simple and effective strategy is proposed for enhancing high-temperature oxidation resistance and corrosion resistance of TiAl-based porous materials. A novel Ti-40Al-10Nb-10Cr porous alloy with controlled lamellar microstructure was fabricated by manipulating a chemical reaction of Ti and Al with Nb and Cr powders. Compared with the Ti-48Al, Ti-48Al-6Nb and Ti-48Al-2Nb-2Cr porous materials, the Ti-40Al-10Nb-10Cr porous alloy exhibited improved high-temperature oxidation resistance (only 6.55 g/m^2 weight gain after thermal cycling treatment at 900 °C/100 h). This indicates that the Ti-40Al-10Nb-10Cr porous alloy could provide expanded opportunities for higher-temperature PM capturing with ultra-high PM removal efficiencies (98.563% for PM$_{>2.5}$, 62.242% for PM$_{<2.5}$). These findings represent an important step toward fabricating TiAl-based porous alloys using powder metallurgy, achieving an excellent high-temperature oxidation resistance due to the unique structure and demonstrating great potential for applications in environment-related fields where highly effective and robust high-temperature filtration is required.

Author Contributions: Conceptualization, W.G. and J.L.; methodology, W.G.; formal analysis, W.G., Y.L., Y.W. and J.L.; data curation, W.G., Z.S. and Y.Z.; writing—original draft preparation, W.G. and J.L.; writing—review and editing, B.L., J.L. and J.Q.; funding acquisition, W.G., J.L. and J.Q. All authors have read and agreed to the published version of the manuscript.

Institutional Review Board Statement: Not applicable.

Informed Consent Statement: Not applicable.

Data Availability Statement: The data that support the findings of this study are available from the first corresponding author upon reasonable request.

Conflicts of Interest: The authors declare no conflict of interest.

References

1. Yang, X.-Y.; Chen, L.-H.; Li, Y.; Rooke, J.C.; Sanchez, C.; Su, B.-L. Hierarchically porous materials: Synthesis strategies and structure design. *Chem. Soc. Rev.* **2017**, *46*, 481–558. [CrossRef] [PubMed]
2. Li, X.; Guan, B.Y.; Gao, S.; Lou, X.W. A general dual-templating approach to biomass-derived hierarchically porous heteroatom-doped carbon materials for enhanced electrocatalytic oxygen reduction. *Energy Environ. Sci.* **2019**, *12*, 648–655. [CrossRef]
3. Liu, J.; Ren, B.; Chen, Y.; Lu, Y.; Zhang, S.; Rong, Y.; Yang, J. Novel design of alumina foams with three-dimensional reticular architecture for effective high-temperature particulate matter capture. *J. Am. Ceram. Soc.* **2019**, *102*, 5576–5586. [CrossRef]
4. Mohanta, K.; Kumar, A.; Parkash, O.; Kumar, D. Low Cost Porous Alumina with Tailored Microstructure and Thermal Conductivity Prepared using Rice Husk and Sucrose. *J. Am. Ceram. Soc.* **2014**, *97*, 1708–1719. [CrossRef]
5. Gui, W.Y.; Liang, Y.F.; Hao, G.J.; Lin, J.P.; Sun, D.Y.; Liu, M.D.; Liu, C.; Zhang, H. High Nb-TiAl-based porous composite with hierarchical micro-pore structure for high temperature applications. *J. Alloys Compd.* **2018**, *744*, 263. [CrossRef]
6. Sun, M.-H.; Huang, S.-Z.; Chen, L.-H.; Li, Y.; Yang, X.-Y.; Yuan, Z.-Y.; Su, B.-L. Applications of hierarchically structured porous materials from energy storage and conversion, catalysis, photocatalysis, adsorption, separation, and sensing to biomedicine. *Chem. Soc. Rev.* **2016**, *45*, 3479–3563. [CrossRef] [PubMed]
7. Li, X.; Lou, L.; Song, W.; Zhang, Q.; Huang, G.; Hua, Y.; Zhang, H.-T.; Xiao, J.; Wen, B.; Zhang, X. Controllably Manipulating Three-Dimensional Hybrid Nanostructures for Bulk Nanocomposites with Large Energy Products. *Nano Lett.* **2017**, *17*, 2985–2993. [CrossRef]
8. Zhang, G.-H.; Zhu, Q.-H.; Zhang, L.; Yong, F.; Zhang, Z.; Wang, S.-L.; Wang, Y.; He, L.; Tao, G.-H. High-performance particulate matter including nanoscale particle removal by a self-powered air filter. *Nat. Commun.* **2020**, *11*, 1653. [CrossRef]
9. Gui, W.Y.; Lin, J.P.; Liang, J.R.; Qu, Y.H.; Guo, Y.C.; Lv, K.; Zhang, H. Micro-/nano-dual-scale porous composite membranes for the separation of nanopollutants from water. *ACS Appl. Nano Mater.* **2019**, *2*, 806. [CrossRef]
10. Kim, H.J.; Park, S.J.; Kim, D.I.; Lee, S.; Kwon, O.S.; Kim, I.K. Moisture effect on particulate matter filtration performance using electro-spun nanofbers including density functional theory analysis. *Sci. Rep.* **2019**, *9*, 7015. [CrossRef]
11. Sharma, P.; Yadav, P.; Ghosh, C.; Singh, B. Heavy metal capture from the suspended particulate matter by Morus alba and evidence of foliar uptake and translocation of PM associated zinc using radiotracer (65Zn). *Chemosphere* **2020**, *254*, 126863. [CrossRef]
12. Aydoğmuş, T.; Palani, D.K.H.; Kelen, F. Processing of porous β-type Ti74Nb26 alloys for biomedical applications. *J. Alloys Compd.* **2021**, *872*, 159737. [CrossRef]
13. Petriev, I.; Pushankina, P.; Bolotin, S.; Lutsenko, I.; Kukueva, E.; Baryshev, M. The influence of modifying nanoflower and nanostar type Pd coatings on low temperature hydrogen permeability through Pd-containing membranes. *J. Membr. Sci.* **2021**, *620*, 118894. [CrossRef]
14. Banhart, J. Manufacture, characterisation and application of cellular metals and metal foams. *Prog. Mater. Sci.* **2001**, *46*, 559–632. [CrossRef]
15. Zhang, H.; Liu, X.; Jiang, Y.; Gao, L.; Yu, L.; Lin, N.; He, Y.; Liu, C. Direct separation of arsenic and antimony oxides by high-temperature filtration with porous FeAl intermetallic. *J. Hazard. Mater.* **2017**, *338*, 364–371. [CrossRef]
16. Kitaoka, S.; Matsushima, Y.; Chen, C.; Awaji, H. Thermal Cyclic Fatigue Behavior of Porous Ceramics for Gas Cleaning. *J. Am. Ceram. Soc.* **2004**, *87*, 906–913. [CrossRef]
17. Voigt, C.; Zienert, T.; Schubert, P.; Aneziris, C.G.; Hubálková, J. Reticulated Porous Foam Ceramics with Different Surface Chemistries. *J. Am. Ceram. Soc.* **2014**, *97*, 2046–2053. [CrossRef]
18. Liu, J.; Li, Y.; Li, Y.; Sang, S.; Li, S. Effects of pore structure on thermal conductivity and strength of alumina porous ceramics using carbon black as pore-forming agent. *Ceram. Int.* **2016**, *42*, 8221–8228. [CrossRef]
19. Han, L.; Li, F.; Deng, X.; Wang, J.; Zhang, H.; Zhang, S. Foam-gelcasting preparation, microstructure and thermal insulation performance of porous diatomite ceramics with hierarchical pore structures. *J. Eur. Ceram. Soc.* **2017**, *37*, 2717–2725. [CrossRef]
20. He, Y.H.; Jiang, Y.; Xu, N.P.; Zou, J.; Huang, B.Y.; Liu, C.T.; Liaw, P.K. Fabrication of Ti–Al Micro/ Nanometer-Sized Porous Alloys through the Kirkendall Effect. *Adv. Mater.* **2007**, *19*, 2102–2106. [CrossRef]
21. Gui, W.; Qu, Y.; Liang, Y.; Wang, Y.; Zhang, H.; Luan, B.; Lin, J. High efficiency hierarchical porous composite microfiltration membrane for high-temperature particulate matter capturing. *NPJ Mater. Degrad.* **2021**, *5*, 1. [CrossRef]

22. Zhang, D.; Wu, J.; Li, B.; Fan, Y. Preparation of ceramic membranes on porous Ti–Al alloy supports by an in-situ oxidation method. *J. Membr. Sci.* **2015**, *476*, 554–560. [CrossRef]

23. Wang, F.; Liang, Y.F.; Shang, S.L.; Liu, Z.K.; Lin, J.P. Phase transformation in Ti-Al-Nb porous alloys and its influence on pore properties. *Mater. Des.* **2015**, *83*, 508. [CrossRef]

24. Kim, D.; Seo, D.; Huang, X.; Sawatzky, T.; Saari, H.; Hong, J.; Kim, Y.-W. Oxidation behaviour of gamma titanium aluminides with or without protective coatings. *Int. Mater. Rev.* **2014**, *59*, 297.

25. Zhao, L.; Li, G.; Zhang, L.; Lin, J.; Song, X.; Ye, F.; Chen, G. Influence of Y addition on the long time oxidation behaviors of high Nb containing TiAl alloys at 900 °C. *Intermetallics* **2010**, *18*, 1586–1596. [CrossRef]

26. Ping, F.-P.; Hu, Q.-M.; Bakulin, A.; Kulkova, S.E.; Yang, R. Alloying effects on properties of Al_2O_3 and TiO_2 in connection with oxidation resistance of TiAl. *Intermetallics* **2016**, *68*, 57–62. [CrossRef]

27. Umakoshi, Y.; Yamaguchi, M.; Sakagami, T.; Yamane, T. Oxidation resistance of intermetallic compounds Al3Ti and TiAl. *J. Mater. Sci.* **1989**, *24*, 1599–1603. [CrossRef]

28. Lin, J.; Zhao, L.; Li, G.; Zhang, L.; Song, X.; Ye, F.; Chen, G. Effect of Nb on oxidation behavior of high Nb containing TiAl alloys. *Intermetallics* **2011**, *19*, 131–136. [CrossRef]

29. Fang, H.; Chen, R.; Chen, X.; Yang, Y.; Su, Y.; Ding, H.; Guo, J. Effect of Ta element on microstructure formation and mechanical properties of high-Nb TiAl alloys. *Intermetallics* **2019**, *104*, 43–51. [CrossRef]

30. Gui, W.Y.; Lin, J.P.; Liu, M.D.; Qu, Y.H.; Wang, Y.C.; Liang, Y.F. Effects of nano-NiO addition on the microstructure and corrosion properties of high Nb-TiAl alloy. *J. Alloys Compd.* **2019**, *782*, 973. [CrossRef]

31. Wu, Y.; Hagihara, K.; Umakoshi, Y. Influence of Y-addition on the oxidation behavior of Al-rich γ-TiAl alloys. *Intermetallics* **2004**, *12*, 519. [CrossRef]

32. Gong, X.; Chen, R.R.; Fang, H.Z.; Ding, H.S.; Guo, J.J.; Su, Y.Q.; Fu, H.Z. Synergistic effect of B and Y on the isothermal oxidation behavior of TiAl-Nb-Cr-V alloy. *Corros. Sci.* **2018**, *131*, 376. [CrossRef]

33. Klein, T.; Rashkova, B.; Holec, D.; Clemens, H.; Mayer, S. Silicon distribution and silicide precipitation during annealing in an advanced multi-phase γ-TiAl based alloy. *Acta Mater.* **2016**, *110*, 236. [CrossRef]

34. Park, S.Y.; Seob, D.Y.; Kim, S.W.; Kim, S.E.; Hong, J.K.; Lee, D.B. High temperature oxidation of Ti-46Al-6Nb-0.5W-0.5Cr-0.3Si-0.1C alloy. *Intermetallics* **2016**, *74*, 8. [CrossRef]

35. Zuo, F.L.; Zhang, S.H.; Liu, H.; Fong, H.; Yin, X.; Yu, J.Y.; Ding, B. Free-standing polyurethane nanofiber/nets air filters for effective PM capture. *Small* **2017**, *13*, 1702139. [CrossRef]

36. Chen, G.L.; Zhang, W.J.; Liu, Z.C.; Li, S.J.; Kim, Y.-W. Microstructure and properties of high-Nb containing TiAl-base alloy. In *Gamma Titanium Aluminides*; Kim, Y.-W., Dimidulk, D.M., Loretto, M.H., Eds.; TMS: Warrendale, PA, USA, 1999; p. 371.

37. Tang, Z.; Shemet, V.; Niewolak, L. Effect of Cr addition on oxidation behavior of Ti-48Al-2Ag alloys. *Intermetallics* **2003**, *11*, 1. [CrossRef]

38. Gui, W.; Liu, J.; Song, X.; Zhang, H.; Lin, J.; Luan, B. A new microfiltration membrane with three-dimensional reticular architecture for Nano-pollutants removal from wastewater. *Prog. Nat. Sci.* **2021**, *31*, 414–419. [CrossRef]

39. Rat'Ko, A.I.; Ivanets, A.I.; Azarov, S.M. Effect of additives on the pore structure of ceramics based on crystalline SiO_2. *Inorg. Mater.* **2008**, *44*, 778–784. [CrossRef]

40. Zhang, R.; Liu, C.; Hsu, P.-C.; Zhang, C.; Liu, N.; Zhang, J.; Lee, H.R.; Lu, Y.; Qiu, Y.; Chu, S.; et al. Nanofiber Air Filters with High-Temperature Stability for Efficient PM2.5 Removal from the Pollution Sources. *Nano Lett.* **2016**, *16*, 3642–3649. [CrossRef] [PubMed]